# Magnetotransport properties of thin Josephson junctions for spectroscopic applications in the presence of large magnetic fields

Citation for the original published paper (version of record):
Trnjanin, N., Cools, I., Buccheri, V. et al (2025). Magnetotransport properties of thin Josephson junctions for spectroscopic applications in the
presence of large magnetic fields. Applied Physics Letters, 127(7).
http://dx.doi.org/10.1063/5.0278518

Applied Physics Letters ARTICLE pubs.aip.org/aip/apl

# Magnetotransport properties of thin Josephson junctions for spectroscopic applications in the presence of large magnetic fields

Cite as: Appl. Phys. Lett. **127**, 072602 (2025); doi: 10.1063/5.0278518
Submitted: 30 April 2025 · Accepted: 29 July 2025 ·
Published Online: 18 August 2025

N. Trnjanin,[a] I. P. C. Cools, V. Buccheri, O. Shvetsov, and T. Bauch

AFFILIATIONS

Department of Microtechnology and Nanoscience, Chalmers University of Technology, 412 96 Gothenburg, Sweden

[a] Author to whom correspondence should be addressed: nermin@chalmers.se

## ABSTRACT

We study thin aluminum Josephson tunnel junctions for spectroscopic applications in high in-plane magnetic fields. These devices, fabricated via a double-angle evaporation process, feature junction stack thickness below 30 nm and lateral dimensions between 80 and 900 nm. Measurements of current–voltage characteristics at 25 mK reveal insights into the Josephson supercurrent, superconducting gap, and inelastic Cooper pair tunneling peaks, driven by the interplay between the ac-Josephson effect and frequency-dependent junction environment impedance. The magnetic field modulation of the Josephson current follows a Fraunhofer pattern for magnetic fields exceeding 1 T, while an on-chip LC electromagnetic mode is probed through the inelastic tunneling peak at fields up to 1.3 T. These findings highlight the robustness of thin aluminum junctions for probing low-energy excitations, such as Andreev bound states, under high magnetic fields, and their potential in quantum device integration and topological state exploration.

Josephson junctions (JJ)s play a fundamental role in a wide range of applications, including photon detection,[1] superconducting quantum interference devices (SQUIDs),[2] qubit technologies,[3] and voltage standardization.[4] They are also useful for probing quantum noise in externally driven two-level systems[5] and shot noise in semiconductor nanowire-based JJs.[6]

JJs also enable detection of microwave-driven transitions between Andreev bound states (ABSs) in superconducting quantum dots via inelastic Cooper pair tunneling (ICPT), seen as distinct peaks in the JJs' current–voltage characteristics (IVCs).[7]

With the emergence of topological superconductivity, unconventional bound states in hybrid JJs—such as Majorana bound states (MBSs)—have gained significant attention for their potential in enabling fault-tolerant quantum computation.[8,9] MBSs arise in hybrid JJs due to the interplay of spin–orbit coupling, strong Zeeman fields, and the superconducting proximity effect, as observed in semiconducting nanowire–superconductor hybrid systems.[10,11]

Probing these exotic bound states requires JJs that remain functional under strong Zeeman fields, up to $\sim 1$ T.

In this paper, we report on the fabrication of thin aluminum (Al) JJs for spectroscopic investigations in large magnetic fields. NbTiN offers high field resilience,[12] but Al enables simpler fabrication and integration via Manhattan-style geometries.[13] Bulk Al (thickness $> 1\,\mu$m) has an in-plane critical field $B_c^{\parallel}$ of 10 mT, but thinning the film raises this limit and provides an additional tuning knob in the form of a large external field.[14–17] For thicknesses $<20$ nm, $B_c^{\parallel}$ can exceed 1 T—sufficient to host Majorana modes in III–V hybrid devices with strong spin–orbit coupling.[10,18,19] Here, we investigate the feasibility of using thin Al JJs under strong $B_{ext}^{\parallel}$ by tracking the ICPT peak, mediated by an on-chip LC circuit, at fields up to 1.3 T.

We fabricated Al JJs of various sizes on two Si chips; Fig. 1(a) shows a representative device with all components. The lateral dimension, $w$, of the square shaped junctions ranges from 80 to 900 nm. First, four 150 nm thick Al bonding pads are deposited. In a second step, Manhattan-type Al JJs are then defined via double-angle evaporation,[13] with junction size set by the width of the two arms. A cross-sectional sketch of the junction stack is shown in the inset of Fig. 1(a). The bottom junction arm has a nominal thickness of $t_b = 13$ nm, and the top junction arm, a nominal thickness of $t_t = 15$ nm. The junction arms are then linked to the bonding pads via 150 nm thick Al patches.

The electrical transport properties of the Al JJs were measured using a 4-point setup [Fig. 1(a)] in a cryogen-free dilution refrigerator

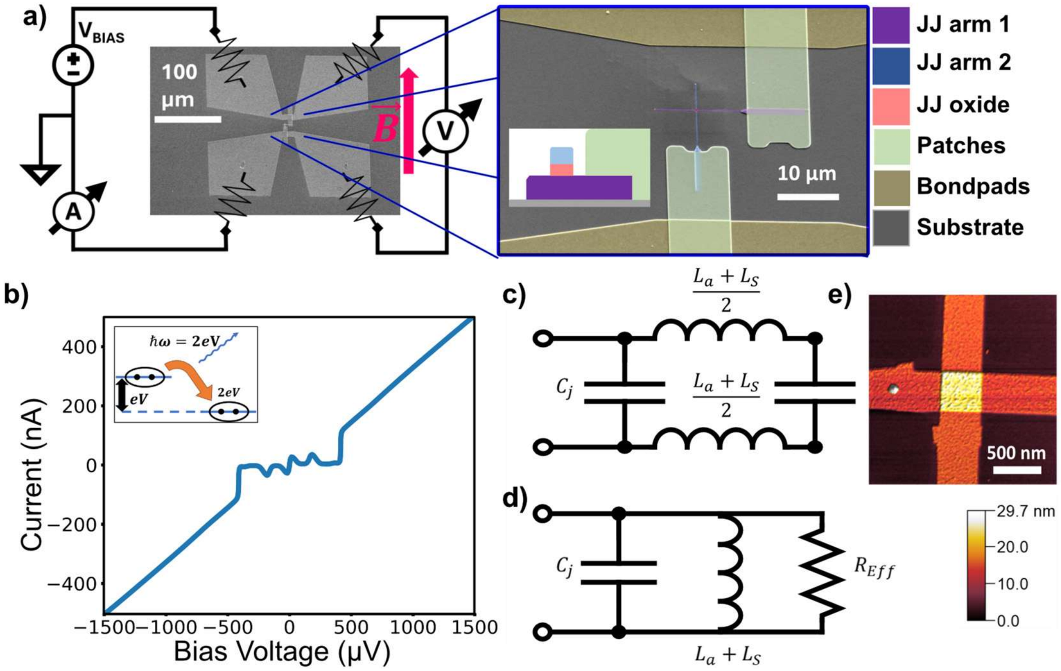

**FIG. 1.** (a) Scanning electron microscopy (SEM) image of the full device together with the measurement circuit setup. The circuit outside the device/chip is represented by impedances connected to the bond pads. In blue box, the zoom in of the central device geometry with different constituents highlighted in false color. Insert: material stack (cross section) of the device. (b) A representative measured current–voltage characteristic at $T = 25$ mK of a $\sim 360 \times 360\,\text{nm}^2$ SIS Al junction, with $2\Delta \sim 400\,\mu$ V. Inset: ICPT process in which Cooper pairs tunnel inelastically and emit energy into the electromagnetic environment.[20–22] (c) Schematic of a circuit representing the electromagnetic environment shunting the JJ. (See main text for details.) (d) Equivalent circuit at high frequencies ($\sim$100 GHz) where $C_S$ effectively behaves as a short. $R_{eff}$ is the effective resistive load as seen by the junction. (e) $2 \times 2\,\mu\text{m}^2$ AFM scan of the junction sandwich area, more details are available in the supplementary material.

(base temperature of 25 mK) with a vector magnet (±1 T in-plane, ±9 T vertical).

First, we characterized the junctions at zero applied magnetic field. A typical IVC of a 360 nm wide junction measured at $T = 25\,\text{mK}$ is shown in Fig. 1(b). We observe four key features: a sharp current increase at $V \approx 400\ \mu\text{V}$ (due to $2\Delta/e$, with $e$ being the elementary charge, and $\Delta$, the superconducting gap); the normal resistance $R_n \approx 3\,\text{k}\Omega$ above $2\Delta/e$; the Josephson supercurrent peak near zero voltage; and a subgap peak at $V \approx 200\ \mu\text{V}$, attributed to ICPT processes.

Using the value of $\Delta$ and $R_n$, we determine the critical current $I_c$ of the junctions from the Ambegaokar–Baratoff relation,[23]

$$I_c = \frac{\pi\Delta}{2eR_n}, \tag{1}$$

which gives $I_c \simeq 116.6\,\text{nA}$ for the 360 nm junction. This value is significantly larger than the height of the Josephson peak near zero voltage, which can be attributed to Josephson phase diffusion processes driven by the Johnson–Nyquist noise from the junction's electromagnetic environment.[24–26] Ivanchenko and Zilberman (I–Z)[27] have addressed this case for an overdamped JJ, modeling the environment as a parallel resistive and capacitive shunt, known as the RCSJ model.[28,29] While a parallel RC shunt is a suitable approximation at low frequencies (see the supplementary material and Fraunhofer analysis below), a more precise treatment of the frequency dependent shunting impedance $Z(\omega)$ is required to accurately capture the ICPT peak around $V \simeq 200\,\mu$ V.

We propose a shunting circuit to model the environment, as shown in Fig. 1(c), consisting of the junction capacitance $C_j$, the junction arm inductance $L_a$, the stray inductance $L_S$ of the bonding pads, and the shunting capacitance $C_S$ of the pads. At 100 GHz, $C_S$ acts as a short (see the supplementary material), simplifying the circuit to the configuration in Fig. 1(d).

In this model, $R_{Eff}$ [see Fig. 1(d)] is an effective resistive load accounting for all high-frequency losses. To determine the values of the RLC components that characterize the electromagnetic environment, shown in Fig. 1(d), we consider the ICPT model [see inset of Fig. 1(b) and S-III supplementary material] to fit the current peak in the IVC at finite voltages. In this scenario, an additional DC-current, $I_{DC}$, arising from the ICPT can flow through the junction at a voltage $V$ smaller than $2\Delta/e$ provided that an electromagnetic environmental mode is available to absorb the outgoing Josephson radiation at frequency $\omega/2\pi = 2eV/h$, where $h$ is the Planck constant.[6,21] This process is described by

$$I_{DC} = \frac{I_c^2 \Re[Z(\omega)]}{2V_{DC}}. \tag{2}$$

Here, $\Re[Z(\omega)]$ is the real part of the junction's electromagnetic environment impedance, which depends on frequency. $I_{DC}$ and $V_{DC}$ are the DC components of the current and voltage, respectively, while $I_c$ is the critical current.

By fitting this model to the IVC for the different junction sizes, we obtain the geometrical dependencies of the shunting inductance, $L = L_S + L_a$, and junction capacitance, $C_j$. To fit the resonance peak at $V \approx 200\,\mu$V, we fix $I_c$ to the Ambegaokar–Baratoff value. A typical fit is shown in Fig. 2(a) as a green dashed line for a 360 nm wide junction. The extracted inductance values shown in Fig. 2(b) are inversely proportional to the junction width $w$ with finite offset $L_S$. This indicates that there are indeed two components to the inductance $L = L_S + L_a$: one constant stray inductance value $L_S$, and $L_a$, which scales with the length and inverse cross section of the junction arms $\frac{l}{wt}$. We consider $L_a = L_{aH} + L_{aV}$ to be the sum of the inductances of the narrow horizontal and vertical junction arms such that $L_a = \mu_0 \lambda^2 \cdot (l_H/w_H t_H + l_V/w_V t_V)$. Here, $\mu_0$ represents the vacuum permeability, $\lambda$ the London penetration depth, $l_{H,V}$ the length, $w_{H,V}$ the width, and $t_{H,V}$ the thickness of each respective arm. The indices H and V refer to the horizontal and vertical junction arm, respectively. We obtain the best fit to the data [see solid line in Fig. 2(b)] by using a stray inductance $L_S \simeq 250$ pH, and for the London penetration depth, $\lambda \simeq 176$ nm. This value is consistent with the expected penetration depth for thin Al films in the dirty limit $\lambda = \lambda_L(0)\sqrt{\xi_0/l} \simeq 200$ nm, with $\lambda_L(0) = 16$ nm and $\xi_0 \simeq 1.6\,\mu$m being the bulk coherence length of Al, and using for the mean free path $l \simeq 9.5$ nm, a value slightly smaller than the film thickness.[30] Furthermore, we attribute $L_s$ to the stray inductance of the bonding pads, which also acts as a big shunting capacitor. Similar values of stray inductance $L_S \simeq 0.2$ nH have been observed in Josephson microwave circuits implementing planar capacitor elements.[31]

In Fig. 2(c), we show the extracted capacitance as a function of junction area $w^2$. The linear scaling $C_j = c_j w^2$, with $c_j \simeq 29\,\mathrm{fF}/\mu\mathrm{m}^2$ (solid line), is typical for Al–AlO$_x$–Al JJs.[32] We attribute the 1.3 fF stray capacitance to the junction arms. The above analysis corroborates that the observed resonance/current peak in the IVCs at finite voltages is mediated by an LC resonance mode involving the junction capacitance and the inductances of the junction arms in series with the stray inductance of the bonding pads.

In the following, we discuss the evolution of the IVC under the application of an $B_{ext}^{\parallel}$ [see field direction in Fig. 1(a)]. In Fig. 3(a), we show a set of IVCs measured at $T = 25$ mK at various applied magnetic fields, ($B_{ext}^{\parallel} = 0$ T to $B_{ext}^{\parallel} = 0.5$ T.) As $B_{ext}^{\parallel}$ is increased, the Josephson and the ICPT peaks diminish and disappear almost completely at $B_{ext}^{\parallel} = 0.5$ T, whereas $\Delta(B)$ shrinks by less than 10%. In the inset of Fig. 3(a), we show the junction current as a function of bias voltage and magnetic field for a wider magnetic field range. For this particular junction, we observe $B_c^{\parallel} \approx 1.6$ T above which the Al electrodes turn normal, consistent with the upper $B_c^{\parallel}$ of thin Al films reported in the literature,[14] and the IVC becomes ohmic and featureless. From the IVC at different magnetic field values, we determine the magnetic field evolution $I_c(B)$ by fitting the I–Z model to the supercurrent peak. Here, we use a modified version of the I–Z model, where the ohmic impedance is replaced by the real part of the frequency-dependent impedance of a parallel RC circuit.[6] At low frequencies, the capacitance $C$ is approximately given by the sum of the junction capacitance and the bonding pad capacitance (see the supplementary material for details). To obtain these $I_c(B)$ values, we first determine the $I_c(B = 0)$ using Eq. (1). Then we fit the modified I–Z model to the supercurrent peak while fixing the critical current to the value obtained from the Ambegaokar–Baratoff equation [see blue solid line data in Fig. 2(a)]. This gives the values of $R_{I-Z} \approx 400\,\Omega$, $C_{I-Z} \approx 20$ fF, and $T_{I-Z} \approx 2$ K for all the devices.[6,27] The R, C, and T values vary less than 10% between devices. The large electron temperature $T_{I-Z}$ is due to the lack of proper electrical filtering at the time of the experiment. To acquire the full $I_c(B)$, we fit the I–Z model to the supercurrent peak data at finite magnetic fields by fixing the values of R, C, and T to the

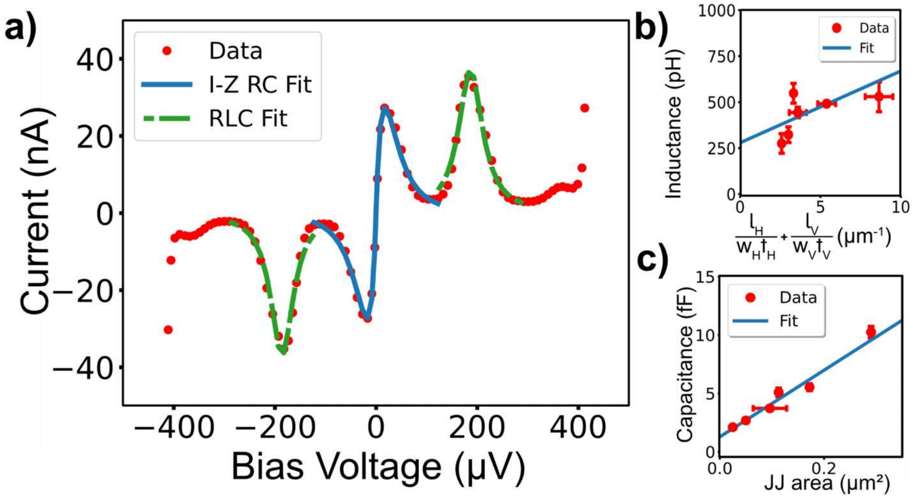

**FIG. 2.** (a) IVC of a 360 nm wide junction at voltages below $2\Delta/e$ at $T = 25$ mK, and $B_{ext} = 0$, featuring a supercurrent peak and current peaks at finite voltages originating from an on-chip $LC$ electromagnetic mode. The Ivanchenko–Zilberman model[27] fit of the measured supercurrent peak around zero bias voltage is shown as the solid blue line (more details concerning the fit in the main text). The dashed green line represents a resonance current peak fit according to Eq. (2). (b) Fitted inductance values $L = L_S + L_a$ (red dots) for the junction geometries, the solid line is a linear fit to the data (see main text for details concerning the fitting). (c) Fitted capacitance values as a function of the square junction area $w^2$ (red dots). The capacitance is a sum of the area dependent junction capacitance and a stray capacitance. The solid line is a linear fit (see the main text for details concerning the fitting).

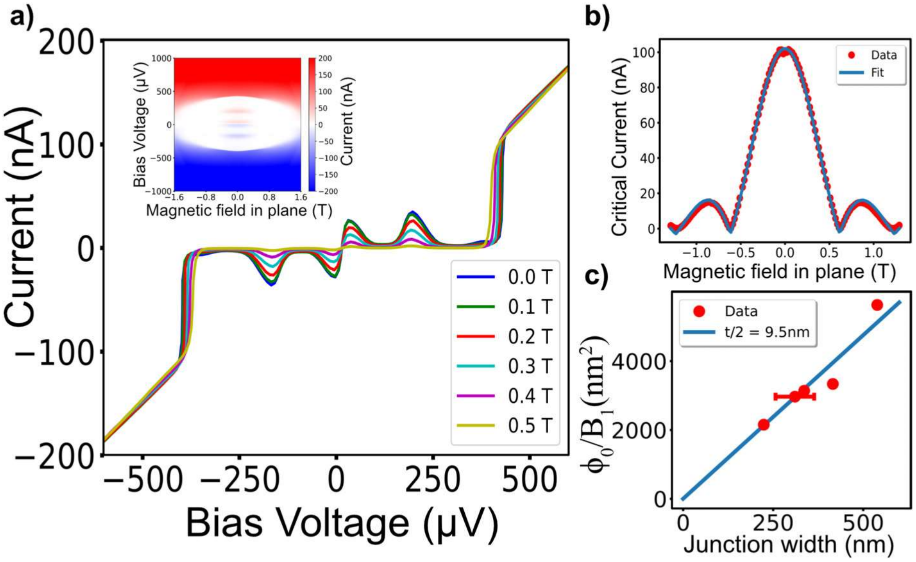

**FIG. 3.** (a) Current–voltage characteristics of a 360 nm wide Al junction at various $B_{ext}^{||}$ parallel to one of the junction arms measured at $T = 25$ mK. Near zero voltage, a thermally broadened Josephson peak is observed. At $V \approx 200\mu$V, an additional peak due to ICPT appears, while above $|2\Delta/e| \simeq 400\,\mu$ V, quasiparticle currents dominate. Both the Josephson and inelastic peaks decrease with increasing magnetic field, along with a reduction in the superconducting gap, $\Delta$. The inset shows a color map of current as a function of bias voltage and magnetic field. (b) $I_c$ as a function of an externally applied $B_{ext}^{||}$ to the junction (red dots). The blue line is a fit to Eq. (3). (c) Effective area as a function of junction width (red dots). The solid line is a linear fit to the data with a slope given by half the junction stack height (see the main text for details). The missing junction sizes< compared to Figs. 2(b) and 2(c), are not included due their minima in the Fraunhofer being outside the range of measurement.

zero field values and varying only $I_c(B)$. In Fig. 3(b), we show the resulting $I_c$ as a function of the $B_{ext}^{||}$ (solid disks) for a 360 nm wide junction, which displays a Fraunhofer pattern. By fitting the expression with a magnetic field-dependent gap correction term to $I_c(B)$,

$$I_c(B) = \frac{\Delta(B)}{\Delta(0)} I_c(0) \left| \frac{\sin(\pi B A_{eff}/\Phi_0)}{\pi B A_{eff}/\Phi_0} \right|, \tag{3}$$

with $B = B_{ext}^{||}$ being the applied in-plane magnetic field, $\Delta(B)$ the magnetic field-dependent superconducting gap value, $A_{eff}$ the effective area of the junction, and $\Phi_0$ the superconductive flux quantum, we obtain the effective area for each junction size.[33,34] The extracted effective areas are shown in Fig. 3(c) as red dots and show that the effective area clearly scales linearly with the width of the junctions. For extremely thin junction electrodes, where the thickness $t \ll \lambda$, $B_{ext}^{||}$ is not effectively screened, allowing the externally applied magnetic field to fully penetrate the superconductor. In this scenario, the effective area can be estimated as $A_{eff} \simeq w t_s/2$.[35] Here, $t_s$ represents the total thickness of the junction stack, including the tunnel oxide layer (see the supplementary material for details). Fitting this expression [blue solid line in Fig. 3(c)] to the effective area, we obtain $t/2 = 9.5$ nm. This is consistent with the thickness of the junction stack (which was measured by AFM to be 24.2 nm on average with $\sigma < 1$ nm across the junctions in the study), taking into account that 4–5 nm of the top Al electrode is oxidized and 1–2 nm is oxidized from the substrate and upward.[36,37]

Finally, we investigate the evolution of the ICPT peak in the IVCs under an applied parallel magnetic field, $B_{\rm ext}^{||}$. Figure 4(a) shows the conductance of a 360 nm wide Al junction for $B_{\rm ext}^{||} > 0.8$ T. As previously shown in Fig. 3(a), we observe a continued reduction in the superconducting gap and an overall increase in subgap conductance with increasing $B_{\rm ext}^{||}$. In the conductance curves, the ICPT current peaks [see Fig. 2(a)] appear as inflection points [see black stars in Fig. 4(a)] that shift to lower voltages with increasing $B_{\rm ext}^{||}$.

We attribute the decrease in the inflection point voltage, $V_r$, or equivalently the resonance frequency of the LC circuit, $f_r = \frac{1}{\sqrt{(L_a+L_s)C_j}}$, to an increase in the kinetic inductance $L_a$ of the junction arms with increasing applied $B_{\rm ext}^{||}$.[38,39] Using $L_s \simeq 0.25$ nH and $C_j = 6$ fF from the analysis shown in Fig. 2, we extract $L_a$ for various magnetic fields. Here, we assume that $L_s$ and $C_j$ are independent of the magnetic field. In Fig. 4(b), we show the normalized variation of the kinetic inductance $\frac{L_a(B)-L_a(0)}{L_a(0)}$ as a function of the magnetic field, which clearly shows a quadratic increase with the applied magnetic field.

To understand the quadratic dependence, we assume[40] that for $T \ll T_c$, we have $L_a(B) \propto 1/T_c(B)$, and therefore $\frac{L_a(B)-L_a(0)}{L_a(0)} = -\frac{T_c(B)-T_c(0)}{T_c(0)}$. An applied magnetic field breaks time-reversal symmetry of the paired electrons, introducing an effective depairing energy $2\alpha$. The reduced critical temperature $T_c(\alpha)$ in the presence of such pair breaking is given by

$$\ln \frac{T_c(\alpha)}{T_c(0)} = \psi\left(\frac{1}{2}\right) - \psi\left(\frac{1}{2} + \frac{\alpha}{2\pi k_B T_c(\alpha)}\right), \tag{4}$$

where $\psi(z) = \Gamma'(z)/\Gamma(z)$ is the digamma function.[33]

For weak depairing (small $\alpha$), expanding around 1/2 yields a linear relation: $k_B[T_c(0) - T_c(\alpha)] = \frac{\pi}{4}\alpha$. In the thin-film limit with an applied parallel field, the depairing parameter is given by $\alpha = \frac{1}{6}\frac{De^2B^2t^2}{\hbar}$, where $D$ is the electronic diffusion constant, and $t$ is the film thickness.[33] Substituting this into the linearized expression

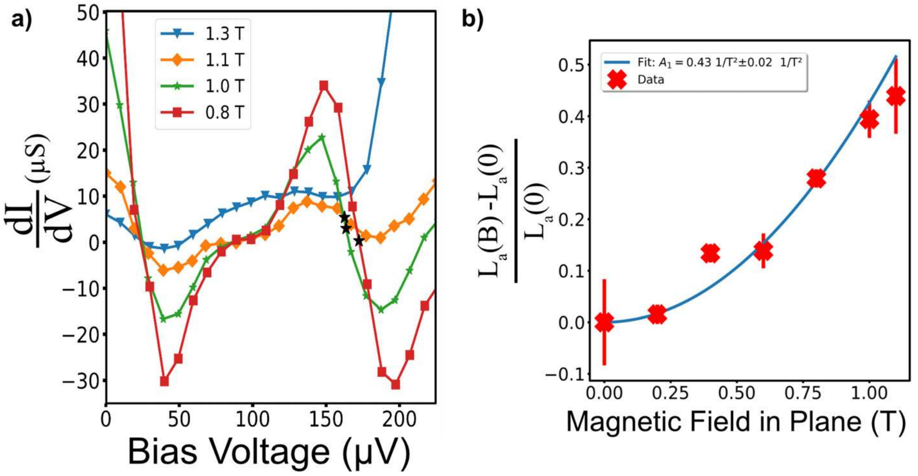

**FIG. 4.** (a) Conductance of a 360 nm wide junction as a function of bias voltage measured at $T = 25$ mK for various externally applied $B_{ext}^{\|}$ above 0.8 T. The black stars represent the inflection points, which corresponds to the voltage position of the on-chip *LC* resonance mode ($V_r$). As $B$ is increased $V_r(B)$ moves toward lower voltages. (b) Shift in kinetic inductance $L_a$ as a function of the applied in-plane magnetic field. The blue line is a fit to Eq. (5) (see the main text for more details). The black stars in (a) correspond to the three rightmost points in (b).

yields a quadratic dependence of the inductance shift on the magnetic field,

$$\frac{L_a(B) - L_a(0)}{L_a(0)} = \frac{\pi}{24} \frac{De^2B^2t^2}{\hbar k_B T_c(0)} = A_1 \cdot B^2. \tag{5}$$

Here, $A_1 = D \cdot t^2 \cdot \frac{1}{T_c(0)} \cdot \frac{\pi e^2}{24\hbar k_B}$. Fitting Eq. (5) to the data in Fig. 4(b), and using $T_c(0) = \Delta(B = 0)/(1.76\, k_B) \approx 1.26\,\mathrm{K}$, where $\Delta(B = 0)$ is extracted from IVCs at $B = 0$, we obtain a diffusion constant $D$ ranging from 19 to 36 cm$^2$/s for thicknesses of 11 and 8 nm, respectively. These values of $D$ are in line with previous findings for thin-film Al of similar thickness.[38,40,41]

The observation of the ICPT in the IVCs at $B_{ext}^{\|} > 1$ T indicates that, at these high field strengths, the ultra-thin Al Josephson junction can still operate effectively as a spectrometer. Such junctions are therefore capable of probing various low-energy excitations, such as ABS excitations[7] at energies below $2\Delta(B)$, which corresponds to approximately 73 GHz at $B_{ext}^{\|} = 1.3$ T.

We have demonstrated that thin Al JJs remain robust and functional for spectroscopy when $B_{ext}^{\|} > 1$ T. The devices maintain superconductivity, exhibiting pronounced Fraunhofer-like modulation of the Josephson current with the applied magnetic field. Moreover, their spectroscopic functionality was confirmed by identifying an on-chip LC resonance mode when $B_{ext}^{\|} > 1$ T, observed through ICPT peaks in the IVC.

The junction operability at these $B_{ext}^{\|}$ highlights their suitability for investigating topological states and low-energy excitations, such as Majorana modes and ABS, in hybrid superconductor–semiconductor or hybrid superconductor–topological insulator systems.[8,42]

See the supplementary material for fabrication and measurement details, a brief description of the ICPT process, a derivation of the transfer function used in the RLC fitting, a simulation of the frequency dependent impedance, which underlies the argument used to reconfigure the effective circuit representing the environment, details concerning the estimation of the effective area extracted from Fraunhofer fits to magnetic field data, details concerning the Ivanchenko–Zilberman current fitting, IVCs of all devices at $B = 0$ T and AFM scans of all devices, and the extracted geometrical parameters.

The devices were fabricated in the MyFab clean room of Chalmers, and we would like to acknowledge the assistance we got from the Nanofabrication Laboratory engineers. We also thank A. Fadavi Roudsari, A. Osman, and others from the Quantum Technology Laboratory for their insights in fabrication. Furthermore, we acknowledge L. Jönssons's contribution in fabricating the mechanical components needed for the experiment. N.T. and I.P.C.C. acknowledge support by the European Union's H2020 research and innovation program, Grant No. 804988 (SiMS). We acknowledge A. Geresdi for providing this funding.

## AUTHOR DECLARATIONS

### Conflict of Interest

The authors have no conflicts to disclose.

### Author Contributions

**N. Trnjanin:** Conceptualization (lead); Data curation (lead); Formal analysis (lead); Investigation (lead); Methodology (lead); Software (lead); Validation (lead); Visualization (lead); Writing – original draft (lead); Writing – review & editing (equal). **I. P. C. Cools:** Conceptualization (supporting); Data curation (supporting); Formal analysis (supporting); Software (supporting); Writing – review & editing (equal). **V. Buccheri:** Formal analysis (supporting); Methodology (supporting); Writing – review & editing (equal). **O. Shvetsov:** Formal analysis (supporting); Validation (supporting); Writing – review & editing (equal). **T. Bauch:** Conceptualization (equal); Data curation (supporting); Formal analysis (supporting); Project administration (equal); Resources (equal); Supervision (lead); Writing – review & editing (equal).

## DATA AVAILABILITY

The data that support the findings of this study are available from the corresponding author upon reasonable request.

## REFERENCES

[1] J. Zmuidzinas and P. L. Richards, "Superconducting detectors and mixers for millimeter and submillimeter astrophysics," Proc. IEEE 92, 1597–1616 (2004).

[2] R. Jaklevic, J. Lambe, A. Silver, and J. Mercereau, "Quantum interference effects in Josephson tunneling," Phys. Rev. Lett. **12**, 159 (1964).

[3] J. Koch, M. Y. Terri, J. Gambetta, A. A. Houck, D. I. Schuster, J. Majer, A. Blais, M. H. Devoret, S. M. Girvin, and R. J. Schoelkopf, "Charge-insensitive qubit design derived from the cooper pair box," Phys. Rev. A **76**, 042319 (2007).

[4] C. A. Hamilton, R. L. Kautz, R. L. Steiner, and F. L. Lloyd, "A practical Josephson voltage standard at 1 V," IEEE Electron Device Lett. **6**, 623–625 (1985).

[5] R. Deblock, E. Onac, L. Gurevich, and L. P. Kouwenhoven, "Detection of quantum noise from an electrically driven two-level system," Science **301**, 203–206 (2003).

[6] D. J. Van Woerkom, A. Proutski, R. J. Van Gulik, T. Kriváchy, D. Car, S. R. Plissard, E. P. Bakkers, L. P. Kouwenhoven, and A. Geresdi, "Josephson radiation and shot noise of a semiconductor nanowire junction," Phys. Rev. B **96**, 094508 (2017).

[7] D. J. Van Woerkom, A. Proutski, B. Van Heck, D. Bouman, J. I. Väyrynen, L. I. Glazman, P. Krogstrup, J. Nygård, L. P. Kouwenhoven, and A. Geresdi, "Microwave spectroscopy of spinful Andreev bound states in ballistic semiconductor Josephson junctions," Nat. Phys. **13**, 876–881 (2017).

[8] C. Nayak, S. H. Simon, A. Stern, M. Freedman, and S. Das Sarma, "Non-Abelian anyons and topological quantum computation," Rev. Mod. Phys. **80**, 1083–1159 (2008).

[9] B. Field and T. Simula, "Introduction to topological quantum computation with non-Abelian anyons," Quantum Sci. Technol. **3**, 045004 (2018).

[10] E. Prada, P. San-Jose, M. W. de Moor, A. Geresdi, E. J. Lee, J. Klinovaja, D. Loss, J. Nygård, R. Aguado, and L. P. Kouwenhoven, "From Andreev to Majorana bound states in hybrid superconductor–semiconductor nanowires," Nat. Rev. Phys. **2**, 575–594 (2020).

[11] A. Laucht, F. Hohls, N. Ubbelohde, M. F. Gonzalez-Zalba, D. J. Reilly, S. Stobbe, T. Schröder, P. Scarlino, J. V. Koski, A. Dzurak *et al.*, "Roadmap on quantum nanotechnologies," Nanotechnology **32**, 162003 (2021).

[12] M. A. Vasyutin, N. D. Kuz'michev, and D. A. Shilkin, "Upper critical field of niobium nitride thin films," Phys. Solid State **58**, 236–239 (2016).

[13] A. Potts, G. Parker, J. Baumberg, and P. De Groot, "CMOS compatible fabrication methods for submicron Josephson junction qubits," IEE Proc.-Sci., Meas. Technol. **148**, 225–228 (2001).

[14] R. Meservey and P. M. Tedrow, "Properties of very thin aluminum films," J. Appl. Phys. **42**, 51 (1971).

[15] R. Meservey and P. Tedrow, "Spin-polarized electron tunneling," Phys. Rep. **238**, 173–243 (1994).

[16] J. Krause, C. Dickel, E. Vaal, M. Vielmetter, J. Feng, R. Bounds, G. Catelani, J. M. Fink, and Y. Ando, "Magnetic field resilience of three-dimensional transmons with thin-film Al/AlO$_x$/Al Josephson junctions approaching 1 T," Phys. Rev. Appl. **17**, 034032 (2022).

[17] A. Schneider, T. Wolz, M. Pfirrmann, M. Spiecker, H. Rotzinger, A. V. Ustinov, and M. Weides, "Transmon qubit in a magnetic field: Evolution of coherence and transition frequency," Phys. Rev. Res. **1**, 023003 (2019).

[18] C. Reeg, O. Dmytruk, D. Chevallier, D. Loss, and J. Klinovaja, "Zero-energy Andreev bound states from quantum dots in proximitized Rashba nanowires," Phys. Rev. B **98**, 245407 (2018).

[19] C. Beenakker, "Search for Majorana fermions in superconductors," Annu. Rev. Condens. Matter Phys. **4**, 113–136 (2013).

[20] G.-L. Ingold and Y. V. Nazarov, "Charge tunneling rates in ultrasmall junctions," in *Single Charge Tunneling: Coulomb Blockade Phenomena in Nanostructures* (Springer, 1992), pp. 21–107.

[21] T. Holst, D. Esteve, C. Urbina, and M. Devoret, "Effect of a transmission line resonator on a small capacitance tunnel junction," Phys. Rev. Lett. **73**, 3455 (1994).

[22] H. Grabert and G.-L. Ingold, "Mesoscopic Josephson effect," Superlattices Microstruct. **25**, 915–923 (1999).

[23] V. Ambegaokar and A. Baratoff, "Tunneling between superconductors," Phys. Rev. Lett. **10**, 486 (1963).

[24] T. Fulton and L. Dunkleberger, "Lifetime of the zero-voltage state in Josephson tunnel junctions," Phys. Rev. B **9**, 4760 (1974).

[25] R. L. Kautz and J. M. Martinis, "Noise-affected I-V curves in small hysteretic Josephson junctions," Phys. Rev. B **42**, 9903 (1990).

[26] W.-S. Lu, K. Kalashnikov, P. Kamenov, T. J. DiNapoli, and M. E. Gershenson, "Phase diffusion in low-$E_j$ Josephson junctions at milli-Kelvin temperatures," Electronics **12**, 416 (2023).

[27] Y. M. Ivanchenko and L. Zil'Berman, "The Josephson effect in small tunnel contacts," Sov. J. Exp. Theor. Phys. **28**, 1272 (1969).

[28] W. Stewart, "Current-voltage characteristics of Josephson junctions," Appl. Phys. Lett. **12**, 277–280 (1968).

[29] D. McCumber, "Effect of ac impedance on dc voltage-current characteristics of superconductor weak-link junctions," J. Appl. Phys. **39**, 3113–3118 (1968).

[30] J. Romijn, T. Klapwijk, M. Renne, and J. Mooij, "Critical pair-breaking current in superconducting aluminum strips far below $T_c$," Phys. Rev. B **26**, 3648 (1982).

[31] I. Siddiqi, R. Vijay, F. Pierre, C. Wilson, L. Frunzio, M. Metcalfe, C. Rigetti, R. Schoelkopf, M. Devoret, D. Vion *et al.*, "Direct observation of dynamical bifurcation between two driven oscillation states of a Josephson junction," Phys. Rev. Lett. **94**, 027005 (2005).

[32] S.-S. Yeh, K.-W. Chen, T.-H. Chung, D.-Y. Wu, M.-C. Lin, J.-Y. Wang, I.-L. Ho, C.-S. Wu, W. Kuo, and C. Chen, "A method for determining the specific capacitance value of mesoscopic Josephson junctions," Appl. Phys. Lett. **101**, 232602 (2012).

[33] M. Tinkham, *Introduction to Superconductivity* (Courier Corporation, 2004).

[34] I. Yanson, "Effect of fluctuations on the dependence of the Josephson current on the magnetic field," Zh. Eksp. Teor. Fiz. **31**, 800 (1970).

[35] J. R. Clem, "Josephson junctions in thin and narrow rectangular superconducting strips," Phys. Rev. B **81**, 144515 (2010).

[36] L. Zeng, D. T. Tran, C.-W. Tai, G. Svensson, and E. Olsson, "Atomic structure and oxygen deficiency of the ultrathin aluminium oxide barrier in Al/AlO$_x$/Al Josephson junctions," Sci. Rep. **6**, 29679 (2016).

[37] L. Chayanun, J. Biznárová, L. Zeng, P. Malmberg, A. Nylander, A. Osman, M. Rommel, P. L. Tam, E. Olsson, P. Delsing *et al.*, "Characterization of process-related interfacial dielectric loss in aluminum-on-silicon by resonator microwave measurements, materials analysis, and imaging," APL Quantum **1**, 026115 (2024).

[38] A. J. Annunziata, D. F. Santavicca, L. Frunzio, G. Catelani, M. J. Rooks, A. Frydman, and D. E. Prober, "Tunable superconducting nanoinductors," Nanotechnology **21**, 445202 (2010).

[39] I. P. Cools, R. M. López-Báez, V. Buccheri, O. Shvetsov, N. Trnjanin, E. Hogedal, and S. P. Dash, "Losses in magnetic field resilient coplanar stripline resonators," J. Phys. D: Appl. Phys. **58**, 255102 (2025).

[40] N. Samkharadze, A. Bruno, P. Scarlino, G. Zheng, D. DiVincenzo, L. DiCarlo, and L. Vandersypen, "High-kinetic-inductance superconducting nanowire resonators for circuit QED in a magnetic field," Phys. Rev. Appl. **5**, 044004 (2016).

[41] A. Anthore, H. Pothier, and D. Esteve, "Density of states in a superconductor carrying a supercurrent," Phys. Rev. Lett. **90**, 127001 (2003).

[42] L. Fu and C. L. Kane, "Superconducting proximity effect and Majorana fermions at the surface of a topological insulator," Phys. Rev. Lett. **100**, 096407 (2008).